Three-dimensional label-free observation of individual bacteria upon antibiotic treatment using optical diffraction tomography

JEONGHUN OH,[1,2] JEA SUNG RYU,[3] MOOSUNG LEE,[1,2] JAEHWANG JUNG,[1,2,6] SEUNGYUN HAN,[1,2] HYUN JUNG CHUNG,[3,4,7] AND YONGKEUN PARK[1,2,5,*] (iD)

[1]*Department of Physics, Korea Advanced Institute of Science and Technology (KAIST), Daejeon, 34141, South Korea*
[2]*KAIST Institute for Health Science and Technology, KAIST, Daejeon 34141, South Korea*
[3]*Graduate School of Nanoscience and Technology, KAIST, Daejeon 34141, South Korea*
[4]*Department of Biological Sciences, KAIST, Daejeon 34141, South Korea*
[5]*Tomocube Inc., Daejeon 34051, South Korea*
[6]*Current Affiliation: Mechatronics R&D Center, Samsung Electronics, Hwasung 18448, South Korea*
[7]*hyunjc@kaist.ac.kr*
[*]*yk.park@kaist.ac.kr*

Abstract: Measuring alterations in bacteria upon antibiotic application is important for basic studies in microbiology, drug discovery, clinical diagnosis, and disease treatment. However, imaging and 3D time-lapse response analysis of individual bacteria upon antibiotic application remain largely unexplored mainly due to limitations in imaging techniques. Here, we present a method to systematically investigate the alterations in individual bacteria in 3D and quantitatively analyze the effects of antibiotics. Using optical diffraction tomography, *in-situ* responses of *Escherichia coli* and *Bacillus subtilis* to various concentrations of ampicillin were investigated in a label-free and quantitative manner. The presented method reconstructs the dynamic changes in the 3D refractive-index distributions of living bacteria in response to antibiotics at sub-micrometer spatial resolution.

1. Introduction

Understanding how antibiotics induce bacterial cell death is essential in the study of microbiology and also to general healthcare in order to help develop, improve, and apply treatment to patients [1]. Over the past years, the mechanism of antibiotics has been studied intensively along with the use of new multiple classes of antibiotics that have succeeded in treating infectious diseases [2]. However, the widespread use of antibiotics has resulted in emergence of drug-resistant bacteria, evoking a significant challenge to the use of antibiotics [3,4]. Since the mainstream approach to overcome this crisis primarily relies on the discovery and development of newer, more efficient antibiotics, understanding how bacteria respond to antibiotics has become more critical.

A basic approach to understanding the mechanism of antibiotics is to observe the phenotypic or physical response of bacteria to antibiotics. Phenotypic imaging has been one of the most popular diagnostic methods to achieve rapid antimicrobial susceptibility testing [5–10], as it provides an easy, low cost, real-time single-cell level examination. Furthermore, phenotypic analysis of bacteria has been exploited to extract useful information in various fields such as epidemiology and systems biology [11]. Although the phenotypic response of bacteria to β-lactam antibiotics has been studied [12,13], detailed phenotypic aspects have been less explored with little available research on the changes in physical quantities such as cell mass, density, and volume. These parameters are direct indicators of cell survival and growth [14,15], which can

provide fundamental insights into the physical and chemical mechanism of bacterial response to antibiotics.

To revisit these unattended but physiologically relevant quantities of bacteria, we need an imaging modality that quantifies the parameters mentioned above. However, conventional two-dimensional (2D) microscopic techniques, such as phase contrast microscopy or differential interference contrast (DIC) microscopy, are not suitable for this purpose, because they are unable to measure three-dimensional (3D) properties. Fluorescence microscopy, such as scanning confocal fluorescence microscopy, allows 3D molecular imaging of cells [16], but the use of fluorescent dyes or proteins have limitations for studying the dynamic alterations in bacteria over a long time due to issues of photo-bleaching and photo-toxicity [17]. Scanning electron microscopy or atomic force microscopy is also not suitable for assessing the dynamics of live bacteria with high throughput [18,19].

To investigate the aforementioned parameters, optical diffraction tomography (ODT), one of the 3D quantitative phase imaging (QPI) techniques, has several potentials [20]. ODT provides a non-invasive and non-contact 3D optical imaging [21]. ODT reconstructs the 3D refractive index (RI) maps of optically transparent samples based on interferometric imaging at multiple illumination angles. Because RI distributi ons serve as both intrinsic cell markers and indicators of protein densities, ODT meets the demands of quantitative phenotypic imaging of unlabeled live cells. Thus, its applications have been rapidly expanded for investigations on hematology [22], microalgae [23], immunology [24], infectious diseases [25,26], plant biology [27], cell biology [27,28], neuroscience [29], and drug discovery [30]. Some bacterial studies have also used ODT [31,32], but its application for bacterial microbiology is in a nascent stage.

In this study, we investigated the 3D bacterial response to antibiotics by exploiting ODT. Our method provides a label-free, real-time analysis of the phenotypic changes in bacterial cells at given antibiotic conditions. The quantitative analysis of 3D RI maps enables examination of the physical changes in cells induced by antibiotic agents. We demonstrate the capability of ODT for imaging the antibiotic response of bacteria in 3D by investigating the response of *Escherichia coli* and *Bacillus subtilis* to a β-lactam antibiotic agent, ampicillin. The dynamics of bacteria were observed by mapping the 3D RI distribution in real time, and the changes in morphological and biochemical parameters were analyzed. With its non-invasive, label-free, and quantitative analysis, our method provides a useful tool for studying and developing antibiotic agents against clinical pathogens that threaten public health.

2. Methods

2.1. Optical diffraction tomography

To measure the 3D RI tomogram of individual bacteria, we employed optical diffraction tomography based on a Mach-Zehnder interferometer equipped with a digital micromirror device (DMD) [Fig. 1(a)].

A coherent laser ($\lambda = 532$ nm in a vacuum; Samba, Cobolt Inc., Sweden) beam was split into a reference beam and sample beam using a 1×2 fiber coupler. The sample beam passed through 4-f relay lenses (L1−3), and was diffracted by a DMD (DLPLCR6500EVM, Texas Instruments Inc., USA). A DMD controlled the angle of the sample beam impinging onto a sample, by displaying digital grating patterns [33]. The time-multiplexing illumination technique was utilized to eliminate the unwanted diffractions of a DMD [34]. The first-order diffraction beam illuminated a sample with a specific incident angle controlled by the pattern projected onto the DMD. The beam diffracted from the DMD passes through a lens (L4) and a condenser lens (NA = 1.2, water immersion, UPLSAPO 60XW, Olympus Inc.) in order to magnify the incident angle. The scattered light from the sample was collected by an objective lens (NA = 1.2, water immersion, UPLSAPO 60XW, Olympus Inc.), and projected to the image plane. At the image plane, the sample beam and reference beam interfere and generate a spatially modulated
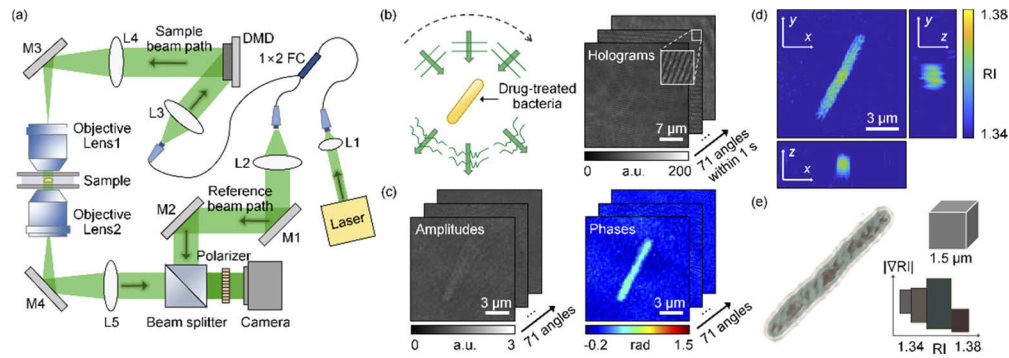
Fig. 1. Measurements of the 3D RI distribution. (a) Experimental setup. M1−M4, mirror; L1−L5, lens; FC, fiber coupler; DMD, digital micromirror device. (b) Sequential illumination scanning for bacteria at 71 illumination angles and the corresponding 71 holograms. (c) Images of the retrieved amplitudes and phases corresponding to the holograms. (d) Three-section view of the reconstructed RI distribution. (e) 3D rendered image of bacteria. The color map shows various colors depending on the value of RI and its gradient value.

hologram pattern, which is recorded using a camera (FL3-U3–13Y3M-C, Point Grey Research Inc.). To combine two beams and generate the interference pattern with the maximum contrast, a beam splitter and a linear polarizer were used, respectively. The beam impinging onto the sample was controlled to have the maximum elevation angle limited by the NA of the condenser lens and was scanned along a full azimuthal angle with 71 steps [Fig. 1(b)]. The total acquisition time for 71 holograms was approximately 1 s (15 ms per hologram).

2.2. Field retrieval and tomogram reconstruction algorithms

The 3D RI distribution of a sample is reconstructed from the measured multiple 2D holograms using the principle of ODT [35,36]. For each hologram pattern, the amplitude and phase delay maps were retrieved using the field retrieval algorithm [Fig. 1(c)] [37,38]. Then, from the retrieved optical field maps with various angles, the 3D RI distribution was determined [Fig. 1(d)]. ODT solves an inverse scattering problem for monochromatic light propagating in a linear, isotropic, and nonmagnetic medium, which satisfies the 3D inhomogeneous Helmholtz equation [35]:

$$(\nabla^2 + k_i^2)\, u_s(\mathbf{r}) = -u(\mathbf{r})f(\mathbf{r})\,, \tag{1}$$

where f is the scattering potential, $f(\mathbf{r}) = k^2 - k_i^2$; k_i and k are the wavevector of the incident field and the diffracted field, respectively; and u_s and u are the scattered field and the diffracted field, respectively. For a slowly varying scattered complex phase, the Rytov approximation can be applied, which has shown better reconstruction performances than the Born approximation [39,40]. According to the Fourier diffraction theorem, each optical field is mapped onto a sphere in the 3D Fourier space [41]. Then, the inverse Fourier transform of the 3D Fourier space provides the RI distribution of the sample [42]. The theoretically calculated lateral and axial resolution of the used optical imaging system is 124 nm and 397 nm, respectively [32,43]. Due to the limited NAs of both the condenser and the objective lens, side scattering signals are not collected, which is known as the missing cone problem. To resolve this missing cone problem, the regularization algorithm based on non-negativity criteria was used [44–46].

2.3. Analysis of cell parameters and visualization methods

To measure cell volumes, the voxels were selected which have an RI higher than a specific value determined by masking the sample region at the initial time for each cell and averaging

the RI values therein. Because the RI value of cell cytoplasm is linearly related to its protein concentration, local protein concentration of a cell can be retrieved from the measured 3D RI tomogram [47,48]. The concentration at each point of the bacteria was determined from RI increment (RII), an increment of an RI in a solution per an increment of concentration in a solute. We assumed that the value of RII is constant inside bacteria, *i.e.* $n(\mathbf{r}) - n_{\text{medium}} = (\text{RII}) \times C(\mathbf{r})$, where n is an RI inside the bacteria, n_{medium} is the RI of surrounding medium, and C is the protein concentration. Therefore, the concentration distribution inside bacteria can be acquired using an RI distribution. In addition, the RII of 0.185 mL/g is known as a typical value for proteins [47,49]. Because many bacteria have proteinaceous organelles [50], it is reasonable that the typical value of RII for proteins could be used in our analysis. The temporal changes in the cellular dry mass are calculated as the total sum of the concentration at each voxel multiplied by its volume. Cytoplasm concentration was calculated by averaging the concentrations at the internal voxels of bacteria.

The 3D rendered image was obtained using commercial software (TomoStudio^TM, Tomocube Inc., Republic of Korea), which delineates the overall RI distributions of bacteria more clearly [Fig. 1(e)]. The different colors indicate the presence of subcellular organelles in bacteria with different RI values, suggesting that our technique provides sub-micrometer spatial resolution to investigate individual bacterial cells.

2.4. Sample preparation

Bacterial strains *Escherichia coli (E. coli*; #1682) and *Bacillus subtilis* (*B. subtilis*; #1021) were purchased from Korean Collection for Type Cultures. *E. coli* cells were cultured in Tryptic soy broth (TSB) and *B. subtilis* were cultured in Nutrient broth (NB). Both bacteria were cultured to the concentration of $1.0-5.0 \times 10^8$ cells/mL to obtain activated bacteria using a nanophotometer (Implen). Centrifugation to wash the cells was repeated twice under the general condition of $8{,}000 \times g$ for 5 minutes at 4°C in 200 μL of PBS solution. Cells were then resuspended in TSB and NB to conduct imaging for the bacteria. Ten microliters of the resuspended solution were placed between two coverslips and then measured using the optical imaging system. All the measurements were performed at room temperature (25°C).

3. Results

In order to systematically investigate the alterations in individual bacteria upon treatment with antibiotics, we measured the 3D RI tomograms of *E. coli* and *B. subtilis* using ODT, and analyzed the measured images.

3.1. Changes in a bacterial cell revealed by time-lapse 3D imaging

We first validated the 3D dynamic imaging capability of ODT by visualizing bacterial growth in the absence of antibiotics. We imaged the dynamics of *E. coli* in growth medium with a time interval of 30 minutes up to 6 hours [Fig. 2].

Both the cross-sections and rendered images of the measured 3D RI tomograms clarify the growth and division of individual *E. coli* [Figs. 2(a) and 2(b)]. Prominent cell division was observed and the increase in the number of *E. coli* over time is presented in Fig. 2(c). The number of *E. coli* doubled constantly at intervals of 56 min, which is consistent with the generation time of *E. coli* at room temperature [51]. These results validate the label-free imaging capability of ODT for studying the responses of individual bacteria.

3.2. Antibiotic responses of Escherichia coli and Bacillus subtilis

Next, we investigated the growth dynamics of individual bacteria under antibiotic treatments. As Gram-positive and Gram-negative models, *E. coli* and *B. subtilis* were selected, respectively. The
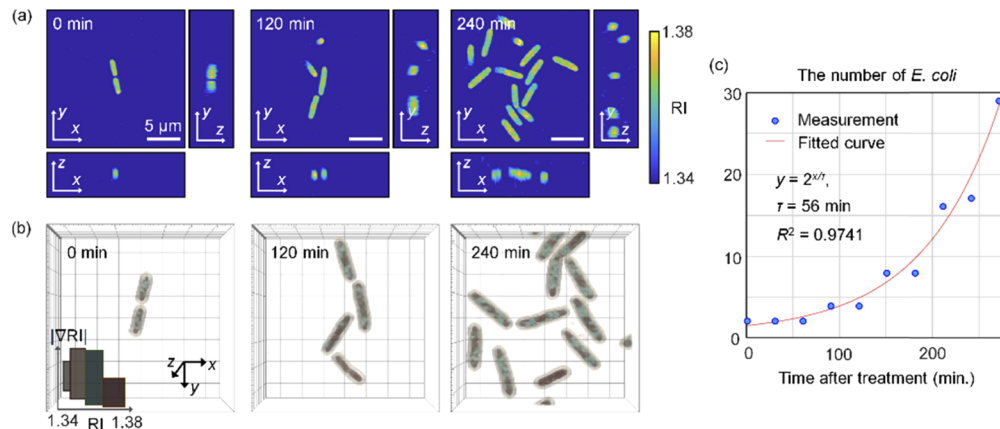
Fig. 2. (a) Three-section views of the reconstructed RI distributions of *E. coli* without antibiotics over time (at 0, 120, and 240 minutes). (b) 3D rendered images of bacteria corresponding to (a). The color map shows various colors depending on the value of the RI. (c) The number of *E. coli* for the control group over time and the fitted curve. R-square = 0.9741.

bacteria were treated with ampicillin at various concentrations of 20, 100, and 300 µg/mL and imaged at time intervals of 30 minutes after drug treatment. As a normal control group, untreated bacterial samples were also measured at the same time intervals.

The results are shown in Fig. 3. In the absence of antibiotic treatment, both *E. coli* and *B. subtilis* exhibited active growth and division. When the bacteria were treated with antibiotics, each cell showed significant morphological alterations, and also presented a decrease in RI values, suggesting cell lysis. To effectively visualize these morphological alterations, the maximum RI projection of each 3D RI tomograms is presented for each group at various time points in Fig. 3.

Figure 3(a) shows the morphological changes in *E. coli*, due to the ampicillin treatment. As the concentration of ampicillin increased, the bacteria underwent earlier cell lysis. From the reconstructed 3D RI tomograms, the point where the RI value drops suddenly could serve as the time point when the bacterial lysis initiated, because the decrease in the RI values of bacteria indicates the efflux of cell cytoplasm. When the concentration of the applied ampicillin was 20, 100, and 300 µg/mL, the bacterial lysis occurred right after 180, 150, and 30 minutes, respectively. In the control group, *E. coli* showed stable growth over time, whereas the bacteria treated with ampicillin did not divide.

In addition, the ampicillin-treated bacteria exhibited distinct elongation of cell shape; the cell length increased without cell division until the point when the RI value increased. Interestingly, the cells exposed to the ampicillin concentration of 20 µg/mL appeared like filaments, exhibiting a fiber-like cell shape. Notably, formation of bulges could be clearly detected in the measured tomograms [the red arrows in Fig. 3(a)]. Bulge formation was observed in groups treated with ampicillin concentrations of 20 or 100 µg/mL. However, a bulge was not formed at 300 µg/mL, which is a significantly high concentration. Furthermore, the rate of cell lysis increased noticeably as the concentration of ampicillin increased to 300 µg/mL.

Compared to the results with *E. coli*, *B. subtilis* exhibited significantly different responses to ampicillin [Fig. 3(b)]. First, the bacterial cell lysis time was earlier than that of *E. coli* treated with low ampicillin concentration. When the ampicillin concentration was 20, 100, and 300 µg/mL, the cell lysis points were conjectured to be right after 90, 90, and 40 minutes, respectively. At an even lower concentration, *B. subtilis* showed faster cell lysis than *E. coli*. In addition, *B. subtilis* exposed to the low concentration of ampicillin (20 µg/mL) did not exhibit morphological
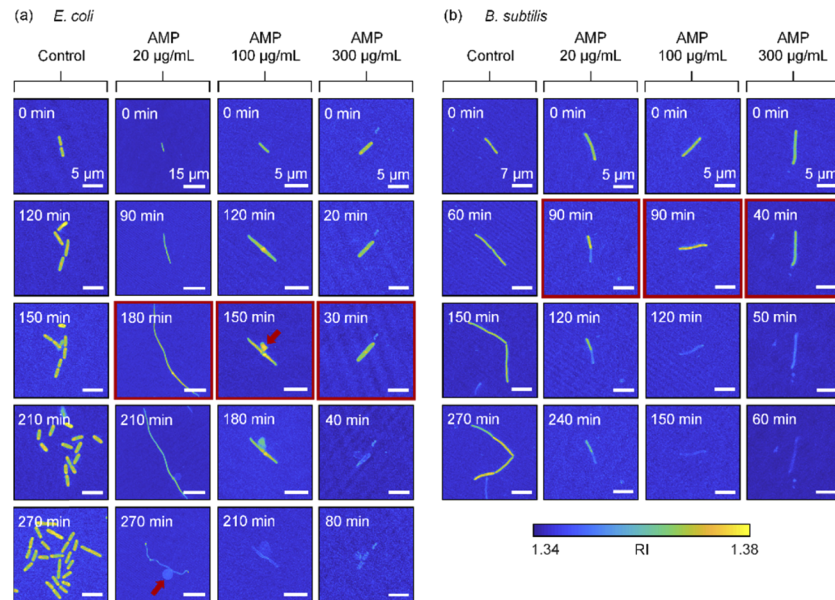
Fig. 3. Maximum RI projection images with ampicillin over time. The red arrows indicate a bulge formed in *E. coli*. The entry with a red border is presumed to be near the point at which the bacteria die. (a) and (b) are *E. coli* and *B. subtilis*, respectively.

alteration into filament-like shapes as observed with *E. coli*. Notably, bulge formation was not observed in *B. subtilis*.

3.3. Quantitative analysis results for morphological and biochemical parameters

To investigate the morphological and biochemical characteristics of bacterial growth under antibiotic treatment, the following cellular parameters were retrieved and analyzed from the measured 3D RI tomograms: cell volume, cellular dry mass, cytoplasm concentration (See Methods). These cellular morphological and biochemical parameters were systematically addressed as a function of time and at various antibiotic concentrations [Fig. 4].

Figure 4(a) shows the cellular volume of *E. coli* over time for various concentrations of ampicillin. Note that this analysis was conducted at the single cell level, and each line in Fig. 4 indicates individual cells. For untreated *E. coli*, cells continued growth and division, and thus the volumes of each cell remained within a certain range ($0.5 - 1.4$ fL). Furthermore, the volumes of untreated *E. coli* oscillated over time, implying continuous growth and division.

Upon ampicillin treatment, *E. coli* did not exhibit cell division, as shown in Fig. 3. The volumes of treated *E. coli* showed monotonic increases, followed by sudden plummets [Fig. 3(a)]. These time points are consistent with the cell lysis observed in the 3D RI tomograms. Comparing the graphs for ampicillin concentrations of 20, 100, and 300 µg/mL, as the concentration of ampicillin increased, the bacteria showed earlier lysis, and the maximum volume of bacteria decreased. In addition, the maximum volume of *E. coli* with ampicillin treatments was significantly larger than that of the control group. These results agree with our observation that when ampicillin is applied, cell division stops and abnormal elongation and bulge formation occurs. This abnormal growth occurred for a shorter time at high ampicillin concentration, indicating that *E. coli* burst to death faster at higher antibiotic concentrations [Fig. 4(b)].

The cellular dry mass of *E. coli* is shown in Fig. 4(c) (See Methods). The graphs for the dry mass are similar to those of cell volume [Fig. 4(a)], indicating that the cytoplasmic concentrations
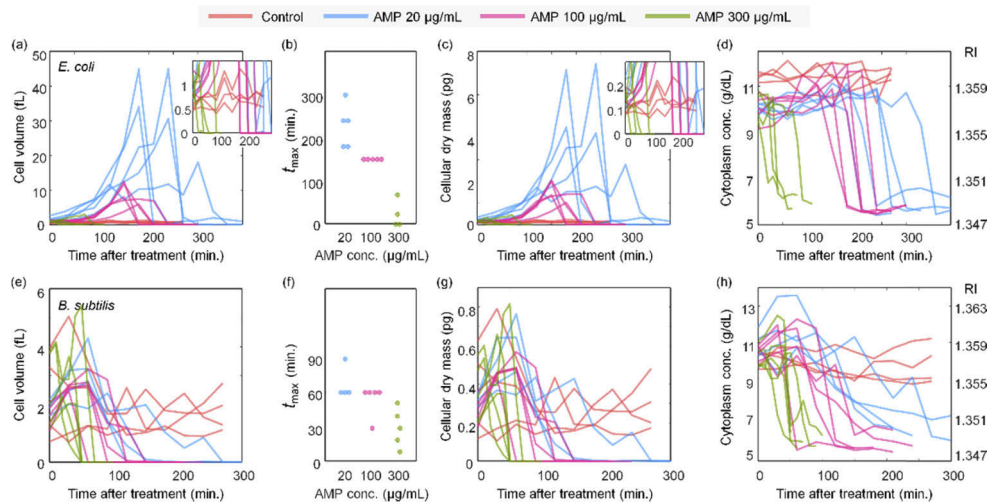
Fig. 4. Cell volume, cellular dry mass, cytoplasm concentration and corresponding RI depending on the concentrations of ampicillin (0, 20, 100, and 300 µg/mL) and time at the maximum volume. (a−d) and (e−h) are *E. coli* and *B. subtilis*, respectively. The number of dataset for *E. coli* (control, 20, 100, and 300 µg/mL) and *B. subtilis* (control, 20, 100, and 300 µg/mL) is 4, 5, 5, 4, 4, 4, 5, and 5, respectively.

did not significantly change over time. This result can also be confirmed from the measured 3D RI tomograms [Fig. 4(d)]. The cytoplasm concentration increased slightly as the bacteria grew. After bacterial lysis, the internal contents escaped beyond the cell wall, and so, the cytoplasm concentration dropped suddenly. Comparison between the control and ampicillin-treated groups clearly indicates that the sudden drop in cytoplasm concentration was only notable in the latter case.

Compared to *E. coli*, *B. subtilis* did not show noticeable increases in either cell volume or dry mass upon ampicillin treatment [Figs. 4(e)–4(g)]. Rather, the bacteria rapidly reached a much smaller cell volume than the initial volume. The most discernible change was observed for the temporal graphs of cytoplasm concentration; a decrease in cytoplasm concentration caused by ampicillin was relatively well observed [Fig. 4(h)].

To clarify the different lysis behaviors between *E. coli* and *B. subtilis*, we reorganized and compared the species-dependent changes in quantitative parameters. Among the various parameters, we chose to compare cell volumes because they showed the most notable difference [Fig. 5]. At ampicillin concentrations of 20 and 100 µg/mL, the difference in cell volume between *E. coli* and *B. subtilis* was remarkable [Figs. 5(a) and 5(b)]. This is because abnormal growth was observed in *E. coli* treated with ampicillin, but no such growth was observed in *B. subtilis*. Moreover, at ampicillin concentrations of 20 and 100 µg/mL, the time to reach a minimal cell volume was shorter for *B. subtilis* than for *E. coli*. In other words, *B. subtilis* appeared to undergo lysis faster than *E. coli*. However, at the concentration of 300 µg/mL [Fig. 5(c)], this tendency was lost. These observations can be seen more clearly in Fig. 5(d), which represents the maximum volume of the bacteria at each concentration as a relative value. These data sufficiently represent how ODT can quantitatively address the dynamics of the antibiotic response of bacteria.
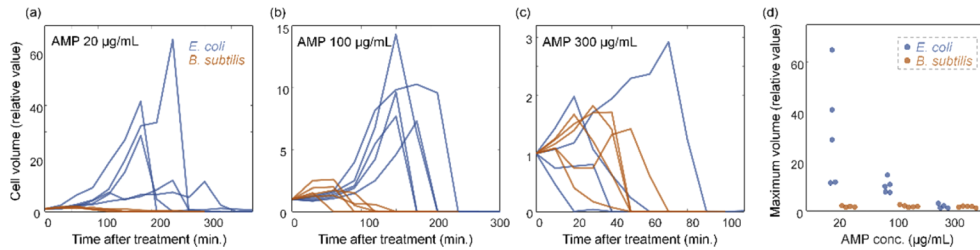
Fig. 5. (a−c) The relative value of cell volume for *E. coli* and *B. subtilis* with the ampicillin concentration of (a) 20 µg/mL (b) 100 µg/mL (c) 300 µg/mL. (d) The relative value of the maximum volume for *E. coli* and *B. subtilis*. The number of dataset for *E. coli* (20, 100, and 300 µg/mL) and *B. subtilis* (20, 100, and 300 µg/mL) is 5, 5, 4, 4, 5, and 5, respectively.

4. Discussions and summary

In summary, we present a method to systematically investigate the alterations in individual bacteria upon antibiotic treatment. Employing ODT, the 3D RI of antibiotic-treated bacteria was measured over time in a label-free and non-invasive manner. The 3D RI reconstruction of *E. coli* and *B. subtilis* bacteria provides the morphological and biochemical parameters related to their real-time alterations depending on the concentration of ampicillin, which were characterized by the inhibition of cell division, bulge formation, abnormal elongation, and cell lysis. Because the RI inside the bacteria is directly related to the cytoplasm concentration, dynamics of cytoplasmic concentrations and cellular dry mass were also analyzed quantitatively. Moreover, we quantitatively deduced the bacterial lysis time through a sudden change in cell volume or cellular dry mass. This can also be used effectively to study the cell cycle of bacteria [52]. Because the presented method is general, it can be used for various applications of microbiology, ranging from bacteria classifications to cell dynamics in the bacterial infection scenarios [53,54].

Our measurements and observations with bacteria are consistent with those in the existing literature. Ampicillin from the β-lactam class inhibits cell wall synthesis, leading to various changes in bacterial cell shape and size, and finally resulting in bacterial cell death [55,56]. It is also intriguing to observe the changes in bacterial appearance depending on the ampicillin concentration. Spratt explains that cell division of *E. coli* is inhibited even at low concentrations of ampicillin, resulting in filamentation of *E. coli*; further, at higher concentrations, a bulge is formed in the middle of *E. coli*, and cell lysis occurs at significantly high ampicillin concentrations [13]. In our experiments, the corresponding concentrations can be considered as 20, 100, and 300 µg/mL, respectively. Comparing the cells with 20 µg/mL of ampicillin to the control group, cell division was inhibited, and abnormal growth, i.e. filamentation, was observed. As the concentration increased to 100 µg/mL, the filamentation phenomenon decreased, and the bulge became more pronounced. This is also consistent with the statement that only lysis was observed at the concentration of 300 µg/mL.

The different responses of *E. coli* and *B. subtilis* to ampicillin are also noteworthy for discussion. Ampicillin hinders transpeptidation by combining with penicillin-binding proteins on maturing peptidoglycan strands, and the resulting reduction in peptidoglycan synthesis causes cell lysis [1,57]. In the case of Gram-positive bacteria including *B. subtilis*, the majority of the cell wall is composed of peptidoglycan; thus, the effect on ampicillin is more pronounced [58], resulting in faster cell lysis. This explains the contrast in the *E. coli* and *B. subtilis* at ampicillin concentrations of 20 and 100 µg/mL. In addition, there is a difference in the reactivity of Gram-positive and Gram-negative bacteria to ampicillin, but ampicillin eventually leads to cell death in both types of bacteria [1]. Our experiments confirmed that both *E. coli* and *B. subtilis* reached cell lysis in

the presence of ampicillin. Indeed, our results were based on small datasets but were sufficient to epitomize the antibiotic response in a label-free, quantitative, and three-dimensional manner.

Previously, 2D QPI techniques have been applied for the study of individual bacteria [59–61]. However, 2D QPI only measures the optical phase delay maps, an integration of RI values along an optical path, and does not provide tomographic measurements of individual bacteria. As demonstrated in this work, ODT enables the systematic investigation of various volumetric information of individual bacteria. We emphasize that the 3D imaging technique exploited here is not limited to the objects targeted in this paper. The species of bacteria and the type of antibiotics can be expanded as needed. In addition, using this method, it is possible to conduct statistical analysis by increasing the number of microbes regardless of single cells or multiple cells. It is also possible to infer the physical functions and biological characteristics of bacteria from their interior structural features [50,62,63]. Moreover, quantitative analysis for other morphological and biochemical parameters can be attempted. For instance, when a bulge is formed in *E. coli*, each volume or cytoplasm concentration can be quantified by separating the bulge and non-bulge portions. The lifetime of the bulge can also be measured. In this case, combination with the segmentation method will serve as the key to analysis [24]. We believe that the methods presented in this paper will provide microbiologists with broader insights into the various responses of bacteria to antibiotics.

Disclosures

Prof. Park and Mr. Moosung Lee have financial interests in Tomocube Inc., a company that commercializes optical diffraction tomography and quantitative phase imaging instruments and is one of the sponsors of the work.

References

1. M. A. Kohanski, D. J. Dwyer, and J. J. Collins, "How antibiotics kill bacteria: from targets to networks," Nat. Rev. Microbiol. **8**(6), 423–435 (2010).
2. O. J. Pambos and A. N. Kapanidis, "Tracking antibiotic mechanisms," Nat. Rev. Microbiol. **17**(4), 201 (2019).
3. R. I. Aminov, "A brief history of the antibiotic era: lessons learned and challenges for the future," Front. Microbiol. **1**, 134 (2010).
4. H. C. Neu, "The crisis in antibiotic resistance," Science **257**(5073), 1064–1073 (1992).
5. J. Conly and B. Johnston, "Where are all the new antibiotics? The new antibiotic paradox," Can. J. Infect. Dis. Med. Microbiol. **16**(3), 159–160 (2005).
6. M. Veses Garcia, H. Antypas, S. Löffler, A. Brauner, H. Andersson-Svahn, and A. Richter-Dahlfors, "Rapid Phenotypic Antibiotic Susceptibility Testing of Uropathogens Using Optical Signal Analysis on the Nanowell Slide," Front. Microbiol. **9**, 1530 (2018).
7. C. Malmberg, P. Yuen, J. Spaak, O. Cars, T. Tängdén, and P. Lagerbäck, "A novel microfluidic assay for rapid phenotypic antibiotic susceptibility testing of bacteria detected in clinical blood cultures," PLoS One **11**(12), e0167356 (2016).
8. J. Choi, J. Yoo, M. Lee, E.-G. Kim, J. S. Lee, S. Lee, S. Joo, S. H. Song, E.-C. Kim, and J. C. Lee, "A rapid antimicrobial susceptibility test based on single-cell morphological analysis," Sci. Transl. Med. **6**(267), 267ra174 (2014).
9. M. Fredborg, F. Rosenvinge, E. Spillum, S. Kroghsbo, M. Wang, and T. Sondergaard, "Rapid antimicrobial susceptibility testing of clinical isolates by digital time-lapse microscopy," Eur. J. Clin. Microbiol. Infect. Dis. **34**(12), 2385–2394 (2015).
10. M. Fredborg, K. R. Andersen, E. Jørgensen, A. Droce, T. Olesen, B. B. Jensen, F. S. Rosenvinge, and T. E. Sondergaard, "Real-time optical antimicrobial susceptibility testing," J. Clin. Microbiol. **51**(7), 2047–2053 (2013).

11. C. Qi, C. W. Stratton, and X. Zheng, "Phenotypic testing of bacterial antimicrobial susceptibility," in *Advanced Techniques in Diagnostic Microbiology* (Springer, 2006), pp. 63–83.

12. B. R. Bochner, L. Giovannetti, and C. Viti, "Important discoveries from analysing bacterial phenotypes," Mol. Microbiol. **70**(2), 274–280 (2008).

13. B. G. Spratt, "Distinct penicillin binding proteins involved in the division, elongation, and shape of Escherichia coli K12," Proc. Natl. Acad. Sci. **72**(8), 2999–3003 (1975).

14. Z. Yao, D. Kahne, and R. Kishony, "Distinct single-cell morphological dynamics under beta-lactam antibiotics," Mol. Cell **48**(5), 705–712 (2012).

15. C. L. Lewis, C. C. Craig, and A. G. Senecal, "Mass and density measurements of live and dead gram-negative and gram-positive bacterial populations," Appl. Environ. Microbiol. **80**(12), 3622–3631 (2014).

16. F. F. Delgado, N. Cermak, V. C. Hecht, S. Son, Y. Li, S. M. Knudsen, S. Olcum, J. M. Higgins, J. Chen, and W. H. Grover, "Intracellular water exchange for measuring the dry mass, water mass and changes in chemical composition of living cells," PLoS One **8**(7), e67590 (2013).

17. A. Jesacher, M. Ritsch-Marte, and R. Piestun, "Three-dimensional information from two-dimensional scans: a scanning microscope with postacquisition refocusing capability," Optica **2**(3), 210–213 (2015).

18. E. C. Jensen, "Use of fluorescent probes: their effect on cell biology and limitations," Anat. Rec. **295**(12), 2031–2036 (2012).

19. M. D. Murtey and P. Ramasamy, "Sample preparations for scanning electron microscopy–life sciences," in *Modern Electron Microscopy in Physical and Life Sciences* (IntechOpen, 2016).

20. Y. Park, C. Depeursinge, and G. Popescu, "Quantitative phase imaging in biomedicine," Nat. Photonics **12**(10), 578–589 (2018).

21. K. El Kirat, I. Burton, V. Dupres, and Y. Dufrene, "Sample preparation procedures for biological atomic force microscopy," J. Microsc. **218**(3), 199–207 (2005).

22. S. E. Koo, S. Jang, Y. Park, and C. J. Park, "Reconstructed Three-Dimensional Images and Parameters of Individual Erythrocytes Using Optical Diffraction Tomography Microscopy," Ann. Lab. Med. **39**(2), 223–226 (2019).

23. C. Cho, K. Nam, Y. H. Seo, K. Kim, Y. Park, J.-I. Han, and J.-Y. Lee, "Study of Optical Configurations for Multiple Enhancement of Microalgal Biomass Production," Sci. Rep. **9**(1), 1723 (2019).

24. M. Lee, Y.-H. Lee, J. Song, G. Kim, Y. Jo, H. Min, C. H. Kim, and Y. Park, "Deep-learning based three-dimensional label-free tracking and analysis of immunological synapses of chimeric antigen receptor T cells," *BioRxiv* 539858 (2019).

25. T. Tougan, J. R. Edula, E. Takashima, M. Morita, M. Shinohara, A. Shinohara, T. Tsuboi, and T. Horii, "Molecular camouflage of Plasmodium falciparum merozoites by binding of host vitronectin to P47 fragment of SERA5," Sci. Rep. **8**(1), 5052 (2018).

26. H. Park, S.-H. Hong, K. Kim, S.-H. Cho, W.-J. Lee, Y. Kim, S.-E. Lee, and Y. Park, "Characterizations of individual mouse red blood cells parasitized by Babesia microti using 3-D holographic microscopy," Sci. Rep. **5**(1), 10827 (2015).

27. C. Park, S. Lee, G. Kim, S. Lee, J. Lee, T. Heo, Y. Park, and Y. Park, "Three-dimensional refractive-index distributions of individual angiosperm pollen grains," Curr. Opt. Photonics **2**(5), 460–467 (2018).

28. S. Oh, C. Lee, D. Fu, W. Yang, A. Li, C. Ran, W. Yin, C. J. Tabin, X. S. Xie, and M. W. Kirschner, "In situ measurement of absolute concentrations by Normalized Raman Imaging," *BioRxiv*, 629543 (2019).

29. S. A. Yang, J. Yoon, K. Kim, and Y. Park, "Measurements of morphological and biophysical alterations in individual neuron cells associated with early neurotoxic effects in Parkinson's disease," Cytometry, Part A **91**(5), 510–518 (2017).

30. S. Kwon, Y. Lee, Y. Jung, J. H. Kim, B. Baek, B. Lim, J. Lee, I. Kim, and J. Lee, "Mitochondria-targeting indolizino [3, 2-c] quinolines as novel class of photosensitizers for photodynamic anticancer activity," Eur. J. Med. Chem. **148**, 116–127 (2018).

31. Y. P. Liu, "Refractive Index Distribution of Single Cell and Bacterium Usingan Optical Diffraction Tomography System," (2016).

32. V. Lauer, "New approach to optical diffraction tomography yielding a vector equation of diffraction tomography and a novel tomographic microscope," J. Microsc. **205**(2), 165–176 (2002).

33. S. Shin, K. Kim, J. Yoon, and Y. Park, "Active illumination using a digital micromirror device for quantitative phase imaging," Opt. Lett. **40**(22), 5407–5410 (2015).

34. K. Lee, K. Kim, G. Kim, S. Shin, and Y. Park, "Time-multiplexed structured illumination using a DMD for optical diffraction tomography," Opt. Lett. **42**(5), 999–1002 (2017).

35. E. Wolf, "Three-dimensional structure determination of semi-transparent objects from holographic data," Opt. Commun. **1**(4), 153–156 (1969).

36. K. Kim, J. Yoon, S. Shin, S. Lee, S.-A. Yang, and Y. Park, "Optical diffraction tomography techniques for the study of cell pathophysiology," *J. Biomed. Photonics Eng.* 020201-1–020201-16 (2016).

37. M. Takeda, H. Ina, and S. Kobayashi, "Fourier-transform method of fringe-pattern analysis for computer-based topography and interferometry," J. Opt. Soc. Am. **72**(1), 156–160 (1982).

38. S. K. Debnath and Y. Park, "Real-time quantitative phase imaging with a spatial phase-shifting algorithm," Opt. Lett. **36**(23), 4677–4679 (2011).

39. Y. Sung, W. Choi, C. Fang-Yen, K. Badizadegan, R. R. Dasari, and M. S. Feld, "Optical diffraction tomography for high resolution live cell imaging," Opt. Express **17**(1), 266–277 (2009).

40. K. Kim, H. Yoon, M. Diez-Silva, M. Dao, R. R. Dasari, and Y. Park, "High-resolution three-dimensional imaging of red blood cells parasitized by Plasmodium falciparum and in situ hemozoin crystals using optical diffraction tomography," J. Biomed. Opt. **19**(1), 011005 (2013).

41. A. Devaney, "Inverse-scattering theory within the Rytov approximation," Opt. Lett. **6**(8), 374–376 (1981).

42. A. J. Devaney, *Mathematical Foundations Oof Imaging, Tomography and Wavefield Inversion* (Cambridge University Press, 2012).

43. C. Park, S. Shin, and Y. Park, "Generalized quantification of three-dimensional resolution in optical diffraction tomography using the projection of maximal spatial bandwidths," J. Opt. Soc. Am. A **35**(11), 1891–1898 (2018).

44. J. Lim, K. Lee, K. H. Jin, S. Shin, S. Lee, Y. Park, and J. C. Ye, "Comparative study of iterative reconstruction algorithms for missing cone problems in optical diffraction tomography," Opt. Express **23**(13), 16933–16948 (2015).

45. R. Gerchberg, "Super-resolution through error energy reduction," Opt. Acta **21**(9), 709–720 (1974).

46. A. Papoulis, "A new algorithm in spectral analysis and band-limited extrapolation," IEEE Trans. Circuits Syst. **22**(9), 735–742 (1975).

47. R. Barer and S. Joseph, "Refractometry of living cells: Part I. Basic principles," J. Cell Sci. **3**, 399–423 (1954).

48. G. Popescu, Y. Park, N. Lue, C. Best-Popescu, L. Deflores, R. R. Dasari, M. S. Feld, and K. Badizadegan, "Optical imaging of cell mass and growth dynamics," Am. J. Physiol. Cell. Physiol. **295**(2), C538–C544 (2008).

49. J. Jung, S.-J. Hong, H.-B. Kim, G. Kim, M. Lee, S. Shin, S. Lee, D.-J. Kim, C.-G. Lee, and Y. Park, "Label-free non-invasive quantitative measurement of lipid contents in individual microalgal cells using refractive index tomography," Sci. Rep. **8**(1), 6524 (2018).

50. S. Tanaka, M. R. Sawaya, and T. O. Yeates, "Structure and mechanisms of a protein-based organelle in Escherichia coli," Science **327**(5961), 81–84 (2010).

51. A. G. Marr, "Growth rate of Escherichia coli," Microbiol. Mol. Biol. R. **55**, 316–333 (1991).

52. W. D. Donachie, "The cell cycle of Escherichia coli," Annu. Rev. Microbiol. **47**(1), 199–230 (1993).

53. U. Neugebauer, C. Große, M. Bauer, B. Kemper, A. Barroso-Pena, A. Bauwens, M. Glueder, M. Woerdemann, L. Dewenter, and C. Denz, "From Infection to Detection: Imaging S. aureus–host interactions," Biomed. Tech. **57**(SI-1 Track-B), 503–506 (2012).

54. G. Kim, D. Ahn, M. Kang, Y. Jo, D. Ryu, H. Kim, J. Song, J. S. Ryu, G. Choi, and H. J. Chung, "Rapid and label-free identification of individual bacterial pathogens exploiting three-dimensional quantitative phase imaging and deep learning," *BioRxiv*, 596486 (2019).

55. H. Cho, T. Uehara, and T. G. Bernhardt, "Beta-lactam antibiotics induce a lethal malfunctioning of the bacterial cell wall synthesis machinery," Cell **159**(6), 1300–1311 (2014).

56. K. F. Kong, L. Schneper, and K. Mathee, "Beta-lactam antibiotics: from antibiosis to resistance and bacteriology," APMIS **118**(1), 1–36 (2010).

57. E. Efstratiou, A. I. Hussain, P. S. Nigam, J. E. Moore, M. A. Ayub, and J. R. Rao, "Antimicrobial activity of Calendula officinalis petal extracts against fungi, as well as Gram-negative and Gram-positive clinical pathogens," Complement. Ther. Clin. Prac. **18**(3), 173–176 (2012).

58. A. Percival, W. Brumfitt, and J. De Louvois, "The role of penicillinase in determining natural and acquired resistance of gram-negative bacteria to penicillins," J. Gen. Microbiol. **32**(1), 77–89 (1963).

59. B. Kemper, Á. Barroso, M. Woerdemann, L. Dewenter, A. Vollmer, R. Schubert, A. Mellmann, G. von Bally, and C. Denz, "Towards 3D modelling and imaging of infection scenarios at the single cell level using holographic optical tweezers and digital holographic microscopy," J. Biophotonics **6**(3), 260–266 (2013).

60. Y. Jo, J. Jung, J. W. Lee, D. Shin, H. Park, K. T. Nam, J.-H. Park, and Y. Park, "Angle-resolved light scattering of individual rod-shaped bacteria based on Fourier transform light scattering," Sci. Rep. **4**(1), 5090 (2015).

61. H. Alanazi, A. Canul, A. Garman, J. Quimby, and A. Vasdekis, "Robust microbial cell segmentation by optical-phase thresholding with minimal processing requirements," Cytometry, Part A **91**(5), 443–449 (2017).

62. W. Van Iterson, "Some features of a remarkable organelle in Bacillus subtilis," J. Cell Biol. **9**(1), 183–192 (1961).

63. J. B. Parsons, S. D. Dinesh, E. Deery, H. K. Leech, A. A. Brindley, D. Heldt, S. Frank, C. M. Smales, H. Lünsdorf, and A. Rambach, "Biochemical and structural insights into bacterial organelle form and biogenesis," J. Biol. Chem. **283**(21), 14366–14375 (2008).